Frontiers in Heat
and Mass Transfer

Tech Science Press

https://doi.org/10.32604/fhmt.2026.081270

ARTICLE

# Numerical Study on Hydrothermal Characteristics and Entropy Generation of Composite Grooves in Various Microchannels

**Guang Wen**[1], **Wenling Liao**[1,2,*], **Shuaimei Lian**[1] and **Pingping Liu**[1,*]

[1]School of Mechanical Engineering, Chengdu Technological University, Chengdu, China
[2]Sichuan Engineering Research Center for Titanium Alloy Advanced Manufacturing Technology, Panzhihua, China

*Corresponding Authors: Wenling Liao. Email: lwlcdtu18@163.com; Pingping Liu. Email: liupp5216@126.com

Received: 27 February 2026; Accepted: 15 April 2026; Published: 31 August 2026

**ABSTRACT:** In this work, FLUENT is used to systematically investigate the effects of two key factors on the hydrothermal performance and entropy generation within a mass flow rate range of 0.3–1.1 g/s: (1) the coupling modes between grooves (simple and composite) and microchannels (straight, convergent, and divergent), and (2) the cross-sectional shape of composite grooves. Results show that, compared with simple grooves, composite grooves induce stronger spiral fluid disturbances between the mainstream and near-wall zones, enhancing direct fluid impingement on groove walls and thus improving the cooling effect on the microchannel. Among the configurations, the coupling of composite grooves and converging microchannels (CG-R-CM) yields the highest Nusselt number ($Nu$ = 2.38) and the lowest entropy production ($S_G$ = 0.0015) at a mass flow rate of 1.1 g/s, albeit with an exponential increase in pressure drop. In contrast, coupling of composite grooves with divergent microchannels (CG-R-DM) effectively reduces pressure drop, achieving a maximum hydrothermal performance (η) of 1.485. Furthermore, modifying the cross-sectional shape of composite grooves significantly improves heat transfer performance with only a slight increase in the pressure drop. The study provides design references for microchannel-composite groove coupling.

**KEYWORDS:** Various microchannels; simple grooves; composite grooves; hydrothermal performance; entropy generation

## 1 Introduction

With rapid technological advancement, electronic devices are increasingly miniaturization and multi-functional. The microchannel heat sink (MCHS), proposed by Tuckerman and Pease [1], is a dedicated heat dissipation technology for microelectronic devices with a compact structure and excellent heat dissipation performance, but, traditional MCHS fails to meet the high-efficiency heat dissipation needs of advancing microelectronics. Extensive optimization has thus been conducted on traditional MCHS to improve heat dissipation efficiency, categorized into active techniques and passive techniques [2]. Passive techniques, which require no additional power and have good implementation effect, have attracted significant attention, including groove introduction [3–5] and fins addition [6–8], microchannel cross-sectional modification [9–11], twisted tape insertion [12–15], nanofluid [16] and multi-layer mini-channel [17,18].

Among the aforementioned passive techniques, microchannel cross-sectional shape modification is the most straightforward to implement. Ho et al. [19] numerically simulated the hydrothermal performance of divergent microchannels with divergence angles of 1.38 and 2.06, showing that divergent microchannels significantly enhance the $Nu$ and reduce pressure drop compared to straight ones, with more pronounced at high flow rates. Khoshvaght-Aliabadi et al. [20] studied convergent and divergent microchannels on supercritical carbon dioxide hydrothermal performance under turbulent conditions, finding convergent microchannels more effective in enhancing the *Nu* and divergent ones in reducing pressure drop. The maximum hydrothermal performance coefficient of microchannels with bidirectional convergence reach 1.56. Sarvar-Ardeh et al. [21] numerically compare the effects of convergent and divergent microchannels on hydrothermal performance and entropy generation, revealing divergent microchannels reduce average *Nu* and pumping pressure, while convergent ones increase both. Qi and Jing [22] integrated experiments and simulations to analyze the effects of the Y-shaped convergent microchannel on the hydrothermal performance, showing a 19.91%–22.59% improvement in performance coefficient at 0.01–0.15 L/min inlet flow rate for 0.7 convergence rate compared to non-convergent ones. Jia et al. [23] numerically investigated the effect of microchannel divergence angles on the hydrothermal performance of gas-liquid Taylor flow, indicating divergent microchannels reduce pressure drop and enhance *Nu* (maximum 37.7% improvement at 0.8°). These studies confirm that compared to straight microchannels, convergent and divergent ones disrupt the flow boundary layer, enhance fluid mixing and heat transfer, but also alter pressure drop.

In addition to microchannel cross-sectional modification, groove introduction on both microchannel wall sides is another effective approach to enhancing hydrothermal performance. Zhu et al. [24] analyzed the effects of arc-shaped grooves with two distribution patterns, sparse-to-dense and dense-to-sparse, on the hydrothermal performance of microchannels. The results indicate that a higher groove density corresponds to a lower local friction coefficient and a higher local *Nu*. Bian et al. [25] conducted an experimental study to analyze the effects of inclined grooves (located at the bottom of MCHS) on boiling heat transfer and flow stability. Their results showed that, compared with smooth MCHS, inclined grooves can increase heat transfer efficiency by up to 18.31% and mitigate flow boiling instability. Lai et al. [26] conducted a detailed analysis of the effects of arc-shaped, rectangular, trapezoidal, and triangular grooves on the heat dissipation efficiency of MCHS. Among these groove geometries, rectangular grooves exhibit excellent heat transfer capability, and the optimized rectangular groove structure can enhance heat transfer performance by 57.1%. Haque et al. [27] found that the alternating arrangement of semi-pendeloque grooves at an angle of 10°–30° can significantly enhance the heat transfer rate of MCHS. Liu et al. [28] performed numerical simulations to analyze the effects of staggered rectangular, trapezoidal, and triangular grooves on the hydrothermal performance of MCHS. Among these, staggered trapezoidal grooves yielded the highest hydrothermal performance, with a corresponding performance coefficient of 1.61. Liu and Duan [29] evaluated the effects of composite structures-consisting of ribs paired with rectangular, triangular, fan-shaped, and trapezoidal grooves-on the hydrothermal performance of microchannels. The results indicate that the composite structure of trapezoidal grooves and ribs exhibits the strongest synergistic effect in enhancing hydrothermal performance. Mao and Gu [30] investigated the effects of six distinct cross-sectional groove geometries at the bottom of microchannels on heat transfer performance via numerical simulations. They found that the square cross-sectional groove induced stronger vortices, thereby yielding the optimal heat transfer efficiency. Wang [31] examined the impact of surface protrusions on the heat transfer performance of microchannels. Their analysis revealed that surface protrusions enhance such performance by augmenting fluid turbulence, as well as inducing fluid impingement on and separation from the wall. Overall, surface grooves in microchannels modify the internal flow field distribution, thereby enhancing fluid-wall impingement and separation effects. This, in turn, improves the heat transfer performance of the microchannels.

Beyond separately analyzing the effects of microchannel cross-sectional shapes or grooves on the hydrothermal performance of microchannels, the coupling effects of grooves and various microchannel configurations on such performance have also been further investigated. Hamza et al. [32] conducted a comparative analysis of the effects of three microchannel configurations-rectangular microchannels, convergent microchannels, and convergent microchannels with rectangular side grooves-on hydrothermal performance. Among these, rectangular microchannels with rectangular side grooves exhibited the best hydrothermal performance. Furthermore, numerical simulation results by Li et al. [33] showed that, at low *Re*, the straight microchannel with inclined grooves exhibited the optimal hydrothermal performance. In contrast, at high *Re*, the divergent microchannel with inclined grooves achieved the best hydrothermal performance. Notably, the coupling of grooves with convergent or divergent microchannels yields superior heat transfer performance compared to that of grooves coupled with straight channels. However, a balance between heat transfer enhancement and the pressure drop must be struck to achieve optimal hydrothermal performance.

Based on the aforementioned literature review, existing studies mainly focus on simple grooves and lack a thorough understanding of how composite grooves affect microchannel heat transfer performance. Convergent and divergent microchannels, derived from straight microchannels, are effective structures for enhancing fluid disturbance intensity. However, they significantly influence pressure drop, particularly convergent ones. Inspired by the above findings, this work proposes coupling composite grooves with convergent or divergent microchannels to significantly improve heat transfer performance while accounting for pressure drop variations. Therefore, this study systematically investigates the effects of coupling modes between grooves (simple and composite) and microchannels (straight, convergent, and divergent) on hydrothermal performance and entropy production within a mass flow rate range of 0.3–1.1 g/s. Additionally, the effects of the cross-sectional shapes of composite grooves on hydrothermal performance and entropy generation are evaluated. Distributions of velocity, streamlines, pressure, and *Nu* are employed to reveal the underlying enhancement mechanisms.

## 2 Numerical Simulation

### *2.1 Geometric Model*

The microchannel heat sink (MCHS) formed by coupling grooves with microchannels is primarily integrated into microelectronic devices via three methods: external cold plate bonding, embedded packaging substrate, and *in-situ* integration on the chip backside. It is widely applied in high heat flux density ($10^5$ W/m$^2$) devices, including CPUs, GPUs, AI chips, and RF devices. This coupled structure is typically fabricated inside cold plates made of copper, silicon, or high thermal conductivity composite materials, and tightly attached to the chip backside using thermal interface materials. The cooling liquid disrupts the boundary layer via the grooves in the coupled channel, thereby achieving efficient heat transfer. As shown in Fig. 1a, the MCHS consists of multiple parallel microchannels fabricated from copper, with a transparent glass cover pressed onto its surface. Owing to the periodic distribution of multiple microchannels along the width direction, only a single microchannel is selected as the simulation domain to conserve computing resources. Grooves are processed at equal intervals on both side walls of the microchannel.

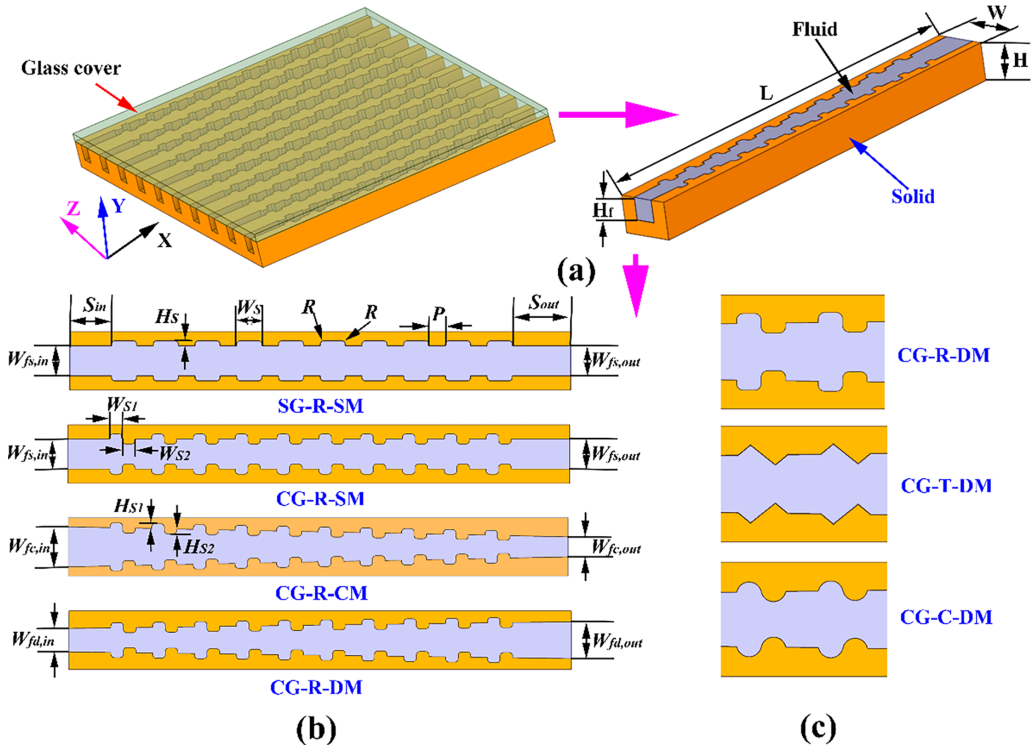


**Figure 1:** The schematic diagram of geometric structure of microchannel, (**a**) three-dimensional structure, (**b**) the coupling modes between grooves and microchannels, (**c**) the cross-sectional shape of composite grooves.

Fig. 1b presents four types of microchannels, which are configured by combining simple grooves, composite grooves, the straight microchannel, the convergent microchannel, and the divergent microchannel. Specifically, these four types include: straight microchannel with simple rectangular grooves (SG-R-SM), straight microchannel with composite rectangular grooves (CG-R-SM), convergent microchannel with composite rectangular grooves (CG-R-CM), and divergent microchannel with composite rectangular grooves (CG-R-DM). Detailed dimensions of these four types of microchannels are shown in Table 1.

**Table 1:** Specific dimensions of each geometric parameter.

| **Parameters** | $L$ | $W$ | $H$ | $H_f$ | $W_{fs,in}$ | $W_{fc,in}$ | $W_{fd,in}$ | $W_{fs,out}$ | $W_{fc,out}$ | $W_{fd,out}$ |
|---|---|---|---|---|---|---|---|---|---|---|
| Value/(mm) | 30 | 3.5 | 2.5 | 1.5 | 1.8 | 2.2 | 1.4 | 1.8 | 1.4 | 2.2 |
| Parameters | $S_{in}$ | $S_{out}$ | $H_S$ | $W_S$ | $H_{S1}$ | $H_{S2}$ | $W_{S1}$ | $W_{S2}$ | R | P |
| Value/(mm) | 2.5 | 3.5 | 0.3 | 1.5 | 0.3 | 0.3 | 0.75 | 0.75 | 0.2 | 1 |

To investigate the influence of cross-sectional differences in composite grooves on hydrothermal performance, two additional configurations of divergent microchannels with composite grooves are designed, including the divergent microchannel with composite triangular grooves (CG-T-DM) and the divergent microchannel with composite circular arc grooves (CG-C-DM), as shown in Fig. 1c. Compared with CG-R-DM, CG-T-DM, and CG-C-DM retain identical dimensions except for differences in their cross-sectional profiles.

### 2.2 Governing Equations

To analyze the influence of microchannel structural parameters on hydrothermal characteristics, the following assumptions are made: the work fluid is incompressible, the fluid flow and heat transfer are in a stable state, and the effects of volume force, viscosity dissipation, and radiative heat transfer are ignored [34]. Based on the above assumptions, the continuity equation and momentum equation can be described as follows.

$$\nabla \cdot \vec{U} = 0 \tag{1}$$

$$\nabla \cdot (\rho_f \vec{U}\vec{U}) = -\nabla P + \nabla \cdot (\mu_f \nabla \vec{U}) \tag{2}$$

The energy equation in the fluid domain and solid domain can be described as:

$$\nabla \cdot (\rho_f c_{p,f} \vec{U} T_f) = \nabla \cdot (k_f \nabla T_f) \text{ (for fluid)} \tag{3}$$

$$k_s \nabla^2 T_s = 0 \text{ (for solid)} \tag{4}$$

In Eqs. (1)–(4), $U$ is the fluid velocity, $\rho$ is the density, $P$ is the pressure, $\mu$ is the dynamic viscosity, $C_p$ is the specific heat, $T$ is the temperature, and $k$ is the thermal conductivity. The subscripts $f$ and $s$ represent fluids and solids, respectively.

In this work, water with constant thermophysical properties is selected as the fluid medium, and the material of the microchannel heat sink is copper. The thermophysical properties of copper and water are shown in Table 2.

**Table 2:** Thermophysical parameters of the copper and water.

| Material | $\rho$ (kg·m$^{-3}$) | $C_p$ (J·kg$^{-1}$·K$^{-1}$) | $k$ (W·m$^{-1}$·K$^{-1}$) | $\mu$ (kg·m$^{-1}$·s$^{-1}$) |
|---|---|---|---|---|
| Water | 998.2 | 4182 | 0.6 | 0.001003 |
| Copper | 8978 | 381 | 387.6 | – |

### 2.3 Boundary Settings

The inlet of the microchannel is defined as a velocity-inlet boundary, with a fixed inlet temperature of 300 K. Given the variations in inlet dimensions across different microchannel configurations, all microchannels are assigned the same inlet mass flow rate, which ranges from 0.3–1.1 g/s. The correlation between mass flow rate and inlet velocity is presented in Table 3.

$$U_x = U_{in}, U_y = U_z = 0, T = T_{in} = 300\,\text{K} \tag{5}$$

The outlet of the microchannel is defined as a pressure-outlet boundary, with a relative outlet pressure of 0 Pa.

$$P_{out} = 0\text{Pa} \tag{6}$$

The fluid and velocity contact surfaces are set as a non-slip interaction boundary. At this boundary, the fluid and solid have the same temperature and heat transfer.

$$\vec{U} = 0,\ T_f = T_s,\ -k_s \frac{\partial T_s}{\partial n} = k_f \frac{\partial T_f}{\partial n} \tag{7}$$

**Table 3:** The correlation between mass flow rate and inlet velocity.

| Mass Flow Rate | 0.3 g/s | 0.5 g/s | 0.7 g/s | 0.9 g/s | 1.1 g/s |
|---|---|---|---|---|---|
| $H_f \times W_{f,in}$ (1.5 mm × 1.4mm) | 0.1431 m/s | 0.2385 m/s | 0.3339 m/s | 0.4293 m/s | 0.5247 m/s |
| $H_f \times W_{f,in}$ (1.5 mm × 1.8 mm) | 0.1113 m/s | 0.1855 m/s | 0.2597 m/s | 0.3339 m/s | 0.4081 m/s |
| $H_f \times W_{f,in}$ (1.5 mm × 2.2 mm) | 0.091 m/s | 0.15178 m/s | 0.2125 m/s | 0.2732 m/s | 0.3339 m/s |

The bottom wall of the microchannel is the heating surface with a fixed heat flux density.

$$q_w = 10^5 \mathrm{w/m^2} \tag{8}$$

Set both sides of the computational domain as symmetric boundary conditions.

$$\frac{\partial T_s}{\partial Z} = 0 \tag{9}$$

The upper wall of the microchannel is a transparent thermal resistance plate, set as an adiabatic boundary condition

$$-k_s \frac{\partial T_s}{\partial n} = 0, -k_f \frac{\partial T_f}{\partial n} = 0 \tag{10}$$

The wall inlet and outlet of the solid computing domain wall are set as adiabatic boundary conditions.

$$k_s \frac{\partial T_s}{\partial n} = 0 \tag{11}$$

### *2.4 Computational Procedure and Data Reduction*

In this study, the fluid flow characteristics and heat transfer efficiency within the MCHS tube are simulated simultaneously. To ensure the required computational accuracy, the pressure-based coupling method is employed to resolve the pressure-velocity coupling problem. The method based on the least squares unit is utilized to compute the gradient of the diffusion term. Momentum and energy are spatially discretized using a second-order upwind scheme. The convergence residuals of all equations are set to $10^{-8}$.

To quantitatively analyze the numerical simulation results, various parameters are defined as follows.

The average Reynolds number ($Re_{ave}$) can be calculated according to the following formula [33]. The corresponding relationship between inlet mass flow rate and $Re_{ave}$ is shown in Table 4.

$$Re_{ave} = \frac{mD_\mathrm{h}}{\mu_{f A_{ave}}} \tag{12}$$

where $m$ is the inlet mass flow rate, $D_\mathrm{h}$ is the hydraulic diameter of the microchannel, and $A_{ave}$ is the average cross-sectional area of the microchannel. According to the refs. [34,35], $D_\mathrm{h}$ is calculated using the following formula.

$$D_\mathrm{h} = \frac{2H_f W_f}{H_f + W_f} \tag{13}$$

where $H_f$ is the height of the microchannel, $W_f$ is the average width of the microchannel, which is equal to the average value of the microchannel inlet and outlet.

**Table 4:** The correlation between mass flow rate and $Re_{ave}$.

| **Mass Flow Rate/(g/s)** | **0.3** | **0.5** | **0.7** | **0.9** | **1.1** |
|---|---|---|---|---|---|
| $Re_{ave}$ | 181.3 | 302.2 | 423 | 543.9 | 664.8 |

The Nusselt number ($Nu_{ave}$) is used to quantitatively describe the heat transfer performance of microchannels, and the calculation formula is:

$$Nu_{ave} = \frac{\mathrm{h}_{ave} D_{\mathrm{h}}}{k_f} \tag{14}$$

where $\mathrm{h}_{ave}$ is the average heat transfer coefficient, which is defined as:

$$\mathrm{h}_{ave} = \frac{qLW}{A_{sf}(T_{b,ave} - T_{f,ave})} \tag{15}$$

where $L$ and $W$ are the length and width of the bottom wall of the microchannel, respectively, $A_{sf}$ is the area and average temperature of fluid and solid coupling surfaces, $T_{b,ave}$ is the average temperature of the heat sink base, $T_{f,ave}$ is the average temperature of the fluid.

The average friction coefficient ($f_{ave}$) is used to describe the flow characteristics in microchannels, which can be defined as [36]:

$$f_{ave} = \frac{2D_{\mathrm{h}} \Delta P}{L \rho_f u_{in}^2} \tag{16}$$

where $\Delta P$ is the pressure drop between the inlet and outlet of the microchannel.

The comprehensive performance of fluid flow and heat transfer in microchannels can be described by thermal enhancement factors ($\eta$), which can be defined as [19,32]:

$$\eta = \frac{Nu_{ave}/Nu_{ave,0}}{(f_{ave}/f_{ave,0})^{1/3}} \tag{17}$$

where $Nu_{ave,0}$ and $f_{ave,0}$ are the average Nusselt number and friction coefficient of the smooth straight microchannel (S-SM), respectively, as shown in Table 5.

**Table 5:** $Nu_{ave,0}$ and $f_{ave,0}$ under different mass flow rate.

| **Mass Flow Rate/(g/s)** | **0.3** | **0.5** | **0.7** | **0.9** | **1.1** |
|---|---|---|---|---|---|
| $Nu_{ave,0}$ | 8.3 | 9.89 | 11.19 | 12.36 | 13.39 |
| $f_{ave,0}$ | 0.412 | 0.278 | 0.219 | 0.185 | 0.163 |

The thermal resistance ($R_T$) is expressed as:

$$R_T = \frac{T_{b,ave} - T_{f,ave}}{qLW} \tag{18}$$

According to the Bejan's entropy generation theory [37], the total entropy generation ($S_p$) consists of two parts: flow entropy generation ($S_F$) and thermal entropy generation ($S_T$), and the calculation formulas are as follows:

$$S_F = \frac{m\Delta P}{\rho_f T_{f,ave}} \tag{19}$$

$$S_T = \frac{qLW\left(T_{b,ave} - T_{f,ave}\right)}{T_{b,ave} T_{f,ave}} \tag{20}$$

$$S_G = S_F + S_T \tag{21}$$

### *2.5 Grid Independence Evaluation and Numerical Method Validation*

Grid independence testing is a critical step prior to conducting numerical simulations, as it balances simulation accuracy and computational cost. In this work, the computational domain is meshed with unstructured grids using FLUENT Meshing. For grid independence validation, CG-R-SM is selected as the test model, under an inlet mass flow rate of 0.5 g/s. Three indicators of average temperature ($T_{b,ave}$) and maximum temperature ($T_{b,\max}$) of the microchannel base, as well as pressure drop ($\Delta P$) are used to evaluate the independence of the grids, as shown in Fig. 2 and Table 6. Compared with the grid of 2.33 million, the relative deviations on $T_{b,ave}$, $T_{b,\max}$, and $\Delta P$ at the grid of 2.73 million are 0.037%, 0.04%, and 0.09%, respectively. This result means that the grid count of 2.33 million can provide sufficient simulation accuracy while minimizing computational cost. The corresponding grid partitioning strategy is adopted as the standard for other microchannel models, which includes a minimum grid size of 0.003 mm, a maximum grid size of 0.05 mm, and a 5-layer boundary layer applied near the wall.

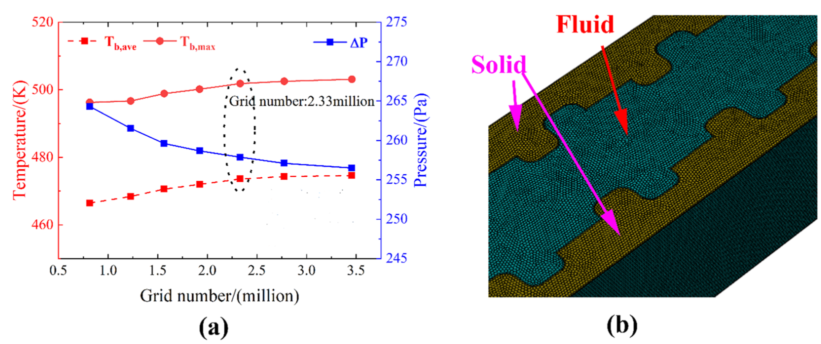


**Figure 2:** (**a**) Grid independence test of CG-R-SM at 0.5 g/s and (**b**) The schematic diagram of the grid structure.

**Table 6:** Effect of grid number on $T_{b,ave}$, $T_{b,\max}$ and $\Delta P$.

| Grids | Grid Number | $T_{b,ave}$ | Diff, % | $T_{b,\max}$ | Diff, % | $\Delta P$ | Diff, % |
|---|---|---|---|---|---|---|---|
| Grid 1 | 814,700 | 316.98 | 0.29 | 320.63 | 0.27 | 253.3 | 1.4 |
| Grid 2 | 1,228,000 | 317.2 | 0.22 | 320.74 | 0.23 | 260.47 | 1.39 |
| Grid 3 | 1,565,000 | 317.45 | 0.14 | 321.06 | 0.13 | 259.6 | 1.05 |
| Grid 4 | 1,922,000 | 317.59 | 0.1 | 321.13 | 0.11 | 257.69 | 0.3 |
| Grid 5 | 2,331,000 | 317.79 | 0.037 | 321.37 | 0.04 | 257.13 | 0.09 |
| Grid 6 | 2,774,800 | 317.91 | Baseline | 321.5 | Baseline | 256.9 | Baseline |

The accuracy of the simulation method is verified before conducting the numerical simulation. Fig. 3a presents a comparison between the numerical simulation results obtained using the present method and the experimental results reported by Ho et al. [19] for rectangular microchannels. The maximum deviations between the numerical simulation results and experimental data for the *Nu* and pressure drop are 4.5% and 3.7%, respectively. As these deviations are much less than 10%, the present simulation method is verified to be reliable for predicting the hydrothermal performance of microchannels. Furthermore, Fig. 3b shows the comparison of *Nu* and $f * Re$ for the microchannel with reentrant cavities between the simulation results and the experimental results reported by Chai et al. [38]. It is evident that a good agreement between the simulation results and experimental results has been observed within the *Re* range of 150 to 650. The maximum deviations of *Nu* and $f * Re$ for simulation results and experimental data are 2.2% and 2.6%, respectively. Therefore, the numerical simulation method employed in this work meets the requirements of computational accuracy.

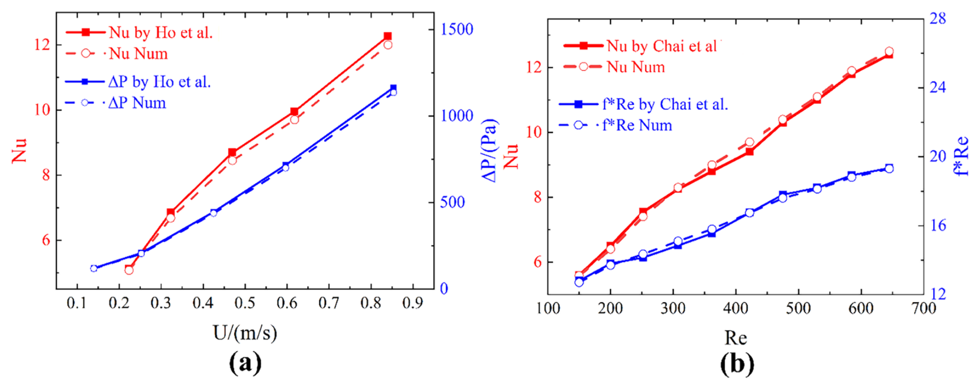


**Figure 3:** Comparison between numerical simulation and experimental results, (**a**) rectangular microchannel and (**b**) microchannel with rectangular cavities.

## 3 Results and Discussion

### *3.1 Effect of Groove Type and Microchannel Pattern*

Fig. 4 compares the velocity distribution of SG-R-SM, CG-R-SM, CG-R-CM, and CG-R-DM on the y = 2 mm plane at 0.7 g/s. For SG-R-SM, the fluid velocity inside the simple groove ranges from 0 to 0.1 m/s, indicating negligible flow within grooves. Consequently, the mainstream fluid has little influence on the fluid trapped in the simple grooves. In addition, the velocity distribution in the mainstream of SG-R-SM is relatively uniform, suggesting extremely weak fluid disturbance. For CG-R-SM, although a large low-velocity zone persists on the upstream side of the composite grooves, a small portion of the mainstream fluid can penetrate into the composite grooves. In addition, the mainstream velocity in CG-R-SM exhibits pulsating fluctuations along the flow direction, periodically inducing fluid separation and attachment on the wall. For CG-R-CM, similar to CG-R-SM, the mainstream fluid still enters the composite grooves. Furthermore, as the microchannel converges along the flow direction, the influence of the mainstream fluid on the fluid inside the composite groove becomes increasingly pronounced. In contrast, for CG-R-DM, the microchannel diverges along the flow direction, leading to a gradual reduction in the influence of the mainstream fluid on the fluid within the composite grooves.

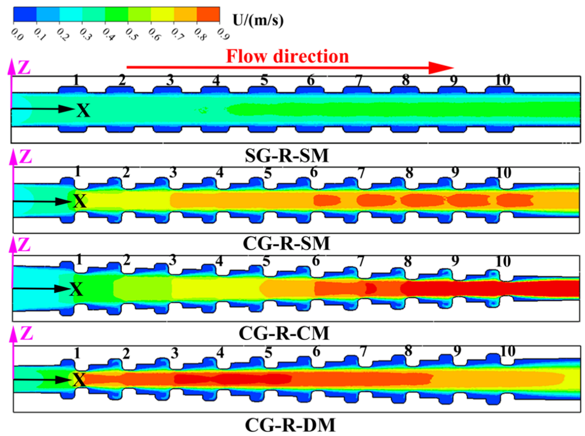


**Figure 4:** Effect of groove and microchannel types on velocity distribution on the y = 2 mm plane at 0.7 g/s.

Fig. 5 compares the two-dimensionless streamline distribution for SG-R-SM, CG-R-SM, CG-R-CM, and CG-R-DM on y = 2 mm, x = 9.5 mm, x = 11.25 mm, and x = 12.875 mm planes at 0.7 g/s. On the y = 2 mm plane, the secondary flow within the simple grooves of SG-R-SM is confined to the groove interior and has little impact on the mainstream. In contrast, for CG-R-SM, CG-R-CM, and CG-R-DM, the fluid inside the composite groove interacts with the fluid on the upstream side to form a larger-scale secondary flow, effectively enhancing fluid mixing between the near-wall and mainstream regions. The planes of x = 8.5, 11.25, and 12.875 mm show that composite grooves induce multiple spiral flows, unlike simple grooves. Specifically, on the x = 12.875 mm plane of CG-R-SM, CG-R-CM, and CG-R-DM, two helical flows cover the entire microchannel cross-section, providing a strong driving force for fluid mixing throughout the microchannel.

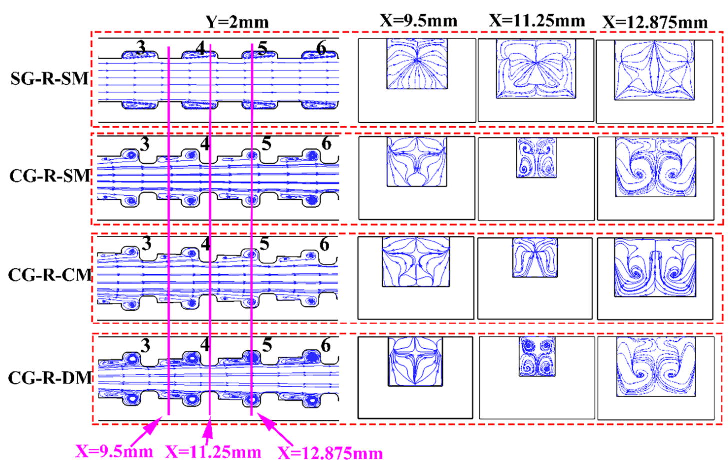


**Figure 5:** Effect of groove and microchannel types on 2D streamline distribution at 0.7 g/s.

Fig. 6 compares the three-dimensionless streamline distribution for four configurations at 0.7 g/s. The 3D streamline reveals that composite grooves generate stronger fluid disturbance than simple grooves. Additionally, in the CG-R-SM, the fluid disturbance intensity near the composite grooves remains nearly constant along the flow direction. In contrast, this intensity gradually increases along the flow direction in CG-R-CM and decreases in CG-R-DM.

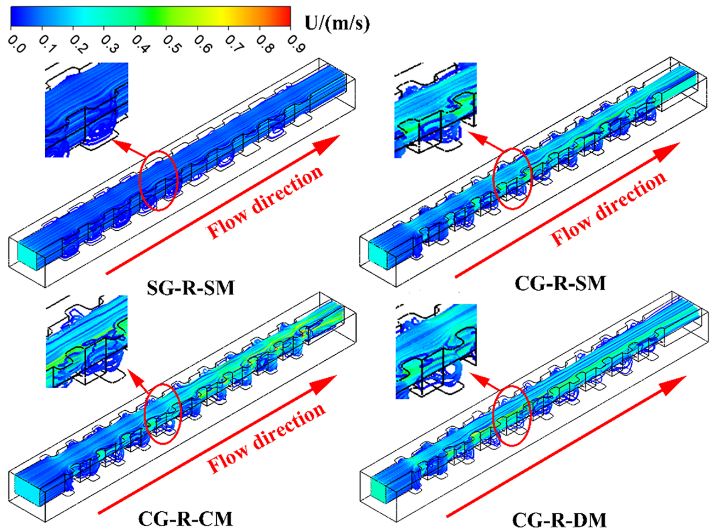


**Figure 6:** Effect of groove and microchannel types on 3D streamline distribution at 0.7 g/s.

Therefore, synthesizing the results presented in Figs. 4–6, composite grooves are more effectively at inducing stronger fluid disturbances than simple grooves. Furthermore, the three microchannel types-straight, convergent, and divergent-primarily alter the distribution of fluid disturbance intensity along the flow direction.

Fig. 7 shows the fluid pressure differences among SG-R-SM, CG-R-SM, CG-R-CM, and CG-R-DM measured on the interface wall at the y = 2 mm and along the mainstream center line. The pressure difference on the interface wall reflects not only the influence of microchannel and groove geometry on pressure fluctuations but also the variation in fluid impingement intensity on the wall. As shown in Fig. 7a, under the condition of consistent outlet pressure, CG-R-CM exhibits the highest inlet pressure, indicating the largest pressure drop. Furthermore, in CG-R-CM, the convergent microchannel causes each composite groove to exert a more significant influence on the amplitude of pressure fluctuations along the flow direction. On the contrary, SG-R-SM has the smallest pressure drop and the smallest pressure fluctuation amplitude. CG-R-SM and CG-R-DM have nearly identical inlet pressures. However, along the flow direction, the pressure in CG-R-SM decreases uniformly, whereas the pressure drop in CG-R-DM gradually diminishes. This is attributed to the gradually weakening fluid impingement on the wall induced by the divergent microchannel in CG-R-DM. Consequently, at 0.7 g/s, the average fluid pressure on the interface wall is highest for CG-R-CM, followed by CG-R-SM, CG-R-DM, and SG-R-SM, respectively. Fluid impingement on the interface wall is strongest in CG-R-DM and weakest in SG-R-SM. Direct fluid impingement on the interface wall helps reduce the thickness of the fluid boundary layer and thereby improve heat transfer efficiency. As shown in Fig. 7b, the variation in fluid pressure along the centerline line is essentially consistent with the pressure fluctuation pattern observed on the interface wall.

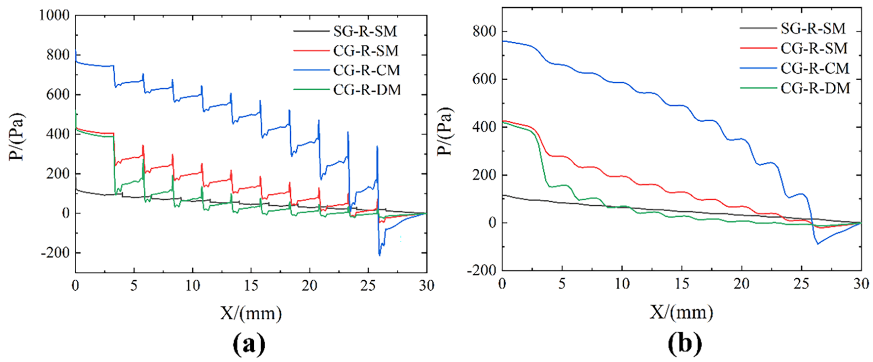


**Figure 7:** Effect of groove and microchannel types on pressure distribution at 0.7 g/s, (**a**) interface wall, (**b**) centerline.

Fig. 8 shows the temperature distribution of SG-R-SM, CG-R-SM, CG-R-CM, and CG-R-DM across different x-planes at 0.7 g/s. For all four microchannel types, the solid domain temperature gradually increases along the flow direction. This is attributed to the gradual rise in fluid temperature, which reduces the temperature difference between the fluid and the solid domain and thereby weakens the convective heat transfer effect [33]. Under the same heat flux density, SG-R-SM exhibits the highest solid domain temperature, indicating that the fluid absorbs the least heat from the solid domain via convective heat transfer. This underlying reason is that the high-temperature near-wall fluid does not mix sufficiently with the low-temperature fluid in the mainstream, making it difficult to enlarge the temperature difference between the solid domain and the near-wall fluid [33]. On the contrary, by increasing the heat transfer area and inducing adequate hot-cold fluid mixing through composite grooves and the converging microchannel, CG-R-CM achieves the lowest solid domain temperature, representing the best convective heat transfer. Furthermore, the solid domain temperature in CG-R-SM is lower than that in CG-R-DM, which is closely related to the larger heat transfer area of CG-R-DM compared to CG-R-SM. In addition to differences in the solid domain, significant differences exist in fluid domain temperature distribution. For the SG-R-SM, from planes P1 to P5, the low-temperature fluid in the mainstream form regular circular zones with a gradually decreasing area. In contrast, for CG-R-SM, CG-R-CM, and CG-R-DM configurations, the shape of the low-temperature fluid zones in the mainstream region varies irregularly across the P1 to P5 planes. This is attributed to the enhanced fluid mixing (in both near-wall and central regions) induced by the spiral flow generated in CG-R-SM, CG-R-CM, and CG-R-DM. On plane P5, the low-temperature fluid zone is the smallest in the CG-R-CM, followed by CG-R-SM, CG-R-DM, and SG-R-SM, in that order.

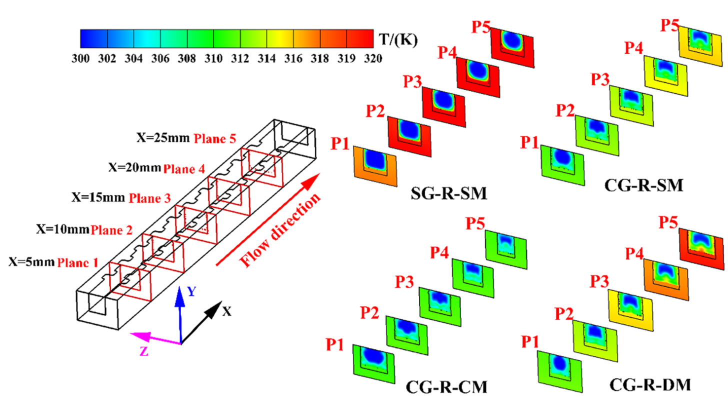


**Figure 8:** Effect of groove and microchannel types on temperature distribution at 0.7 g/s.

Fig. 9a–c shows the effect of groove pattern and microchannel type on $\Delta P$, $T_{b,ave}$, and $R_T$. As shown in Fig. 9a, $\Delta P$ increase with the rise in inlet mass flow rate. Specifically, the variation trends of $\Delta P$ with increasing inlet mass flow rate can be divided into three categories. Among them, CG-R-CM shows the fastest increase in $\Delta P$, which is attributed to the fluid blockage effect caused by the convergent microchannel. For CG-R-SM and CG-R-DM, the $\Delta P$ variation rates are nearly identical at 0.3–0.7 g/s. At 0.7–1.1 g/s, the $\Delta P$ in CG-R-SM is slightly higher than that in CG-R-DM, and the difference grows as increasing flow rate, indicating that divergent channels are more advantageous in reducing $\Delta P$ at high flow rates. Similarly, the $\Delta P$ variation rates in S-SM and SG-R-SM are almost the same, suggesting that simple grooves have little effect on mainstream fluid flow, consistent with the results presented in Fig. 4. As shown in Fig. 9b, $T_{b,ave}$ decrease with increasing mass flow rate due to the reduced boundary layer thickness and enhanced convective heat transfer. Additionally, CG-R-CM yields the lowest $T_{b,ave}$, followed by CG-R-SM, CG-R-DM, SG-R-SM, and S-SM. Specifically, compared with S-SM, the average $T_{b,ave}$ of SG-R-SM, CG-R-SM, CG-R-CM, and CG-R-DM decreased by 0.3%, 2.8%, 3.3%, and 2%, respectively. Therefore, under the same heat flux, CG-R-CM exhibits a lower average solid domain temperature, indicating superior heat transfer performance. As shown in Fig. 9c, increasing fluid velocity effectively reduces boundary layer thickness, thereby decreasing the convective thermal resistance. Composite grooves reduce the average $R_T$ by more than 50% compared with simple grooves, attributed to the composite grooves inducing stronger secondary flow and more intense fluid impingement on the groove walls.

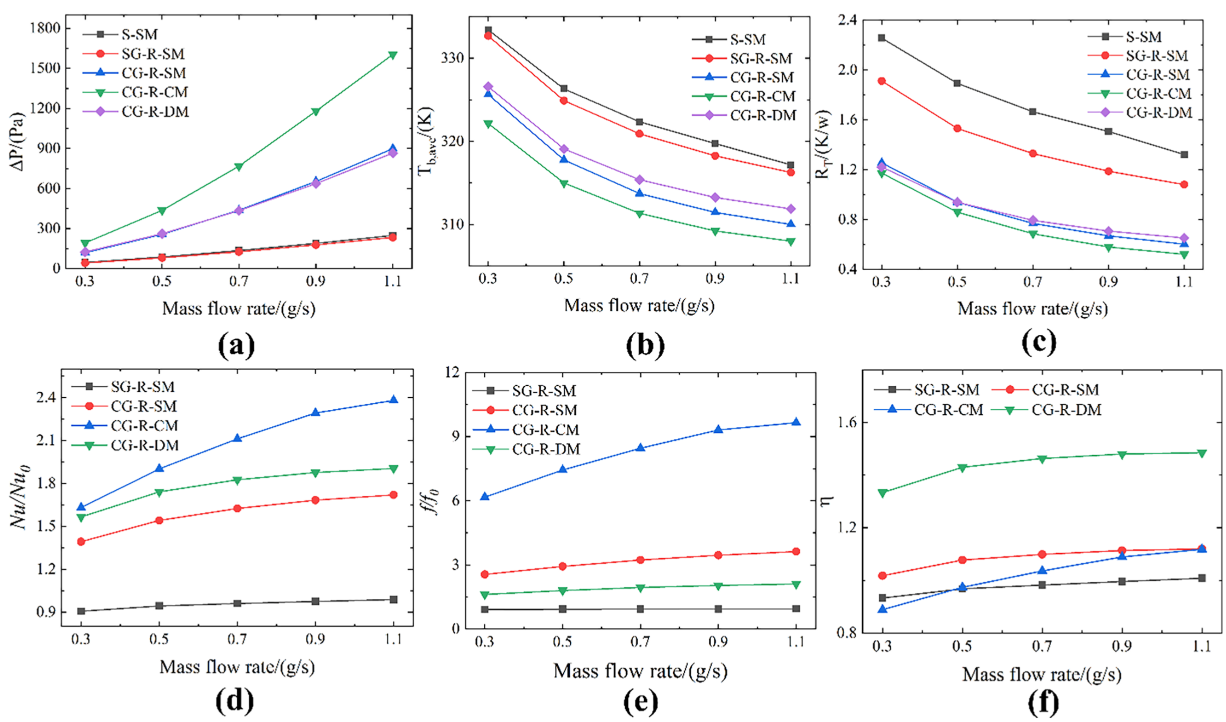


**Figure 9:** Effect of groove and microchannel types on hydrothermal performance indicators, (**a**) $\Delta P$, (**b**) $T_{b,ave}$, (**c**) $R_T$, (**d**) $Nu/Nu_0$, (**e**) $f/f_0$ and (**f**) $\eta$.

Fig. 9d–f illustrates the effects of groove types and microchannel patterns on the ratios of $Nu/Nu_0$, $f/f_0$, and $\eta$. As shown in Fig. 9d, the $Nu/Nu_0$ ratio exhibits an increasing trend with the rise in inlet mass flow rate. Within the mass flow rate range of 0.3–1.1 g/s, the $Nu/Nu_0$ ratio ranges from 0.92 to 1.0 for simple grooves and from 1.39 to 2.38 for composite grooves. indicating that composite grooves provide significantly greater heat transfer performance enhancement. Among these, CG-R-CM shows the fastest increase in $Nu/Nu_0$, reaching a maximum of 2.38 at 1.1 g/s. In addition, the $Nu/Nu_0$ ratio of CG-R-SM is lower than that of CG-R-DM, indicating better convective heat transfer effect in CG-R-DM. This is attributed to the differences in the intensity of fluid impingement on the wall, which corresponds to the pressure variation trends presented in Fig. 9a. As shown in Fig. 9e, the $f/f_0$ ratio of CG-R-CM is significantly higher than those of CG-R-DM, CG-R-SM, and SG-R-SM. Specifically, compared to SG-R-SM, CG-R-SM, and CG-R-DM, the $f/f_0$ ratio of CG-R-CM has increased by over 100%. This indicates that CG-R-CM incurs a substantial pressure drop penalty while enhances heat transfer performance. Additionally, the $f/f_0$ ratio of CG-R-DM is lower than that of CG-R-SM across all mass flow rates, demonstrating the advantage of divergent microchannels in reducing flow resistance. As shown in Fig. 9f, the η is the highest for CG-R-DM across the entire flow range, followed by CG-R-SM, SG-R-SM, and CG-R-CM. Although CG-R-CM delivers the strongest heat transfer enhancement, the proportional increase in pressure drop prevents it from achieving the best overall hydrothermal performance. On the contrary, CG-R-DM achieves a favorable balance, with a maximum η of 1.485 at 0.7 g/s.

Fig. 10 shows the influence of coupling between microchannel and groove on entropy generation. As shown in Fig. 10a, the variation in $S_F$ among SG-R-SM, CG-R-SM, CG-R-CM, and CG-R-DM follows a pattern similar to that of $\Delta P$ in Fig. 9a, which is related to the maximum fluid flow resistance and local fluid disturbance in CG-R-CM. As shown in Fig. 10b, the $S_T$ of SG-R-SM is significantly higher than those of CG-R-SM, CG-R-CM, and CG-R-DM. Specifically, compared with SG-R-SM, the $S_T$ of CG-R-SM, CG-R-DM, and CG-R-CM decreased by more than 25%. This indicates that SG-R-SM has the largest solid-fluid domain temperature difference, leading to the strongest irreversibility in the heat transfer, which aligns with the results shown in Fig. 9d. As the $S_T$ is more than three orders of magnitude higher than the $S_F$, the variation pattern of $S_G$ with mass flow rate is analogous to that of $S_T$, as shown in Fig. 10c. Compared with S-SM, the average $S_G$ of SG-R-SM, CG-R-SM, CG-R-CM, and CG-R-DM decreased by 10%, 51%, 55%, and 50%, respectively. Specifically, at 0.9 g/s, CG-R-CM achieves the minimum $S_G/S_{G0}$ ratio of 0.4. Therefore, secondary flows periodically disrupt and thin the thermal boundary layer, reduce local temperature gradients across the channel, and homogenize fluid temperature distribution. Consequently, the entropy generation caused by heat transfer decreases significantly. Although flow entropy generation increase slightly due to extra shear from vortices, the reduction in thermal entropy generation dominates, leading to an overall decrease in total entropy generation and lower thermodynamic irreversibility.

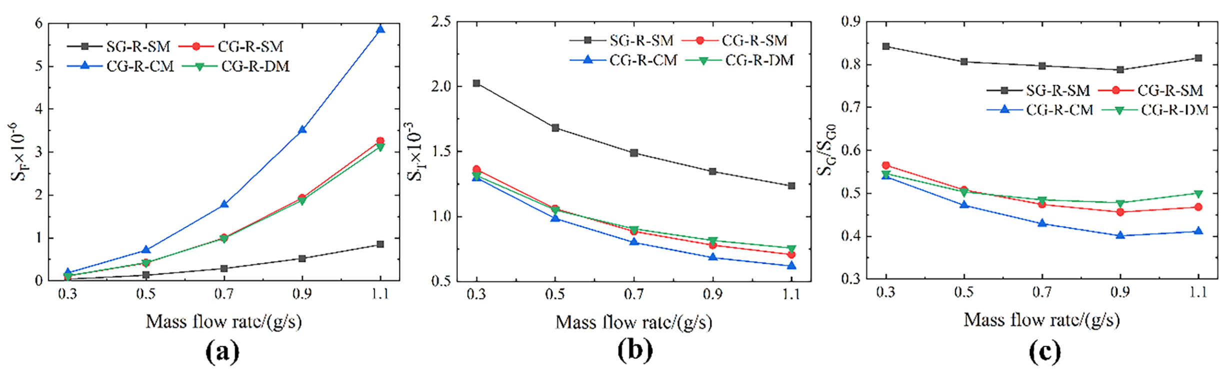


**Figure 10:** Effect of groove and microchannel types on entropy generation indicators, (**a**) $S_F$, (**b**) $S_T$ and (**c**) $S_G/S_{G0}$.

### *3.2 Effect of Composite Groove Cross-Section*

Based on the aforementioned research findings, coupling composite grooves with the divergent microchannel effectively balances heat transfer enhancement and fluid pressure drop reduction, thereby achieving the optimal overall hydrothermal performance. Building on this conclusion, future work analyzes the influence of the cross-sectional shape of composite grooves on hydrothermal performance.

Fig. 11 compares the velocity distribution of CG-R-DM, CG-T-DM, and CG-C-DM on the y = 2 mm plane at 0.7 g/s. In the CG-R-DM, the mainstream fluid mixes with the fluid inside the composite rectangular grooves (labeled 1–8) at the upstream side of these grooves. In the CG-C-DM, this mixing phenomenon is confined to the composite circular grooves (labeled 1–5). In the CG-T-DM, such mixing occurs only within the composite triangular grooves (labeled 1–3). Therefore, along the flow direction, the composite rectangular grooves exhibit stronger fluid disturbance and mixing effects on the near-wall fluid than the composite circular grooves and composite triangular grooves. This phenomenon is conducive to enhancing hot-cold fluids mixing throughout CG-R-DM and promoting convective heat transfer.

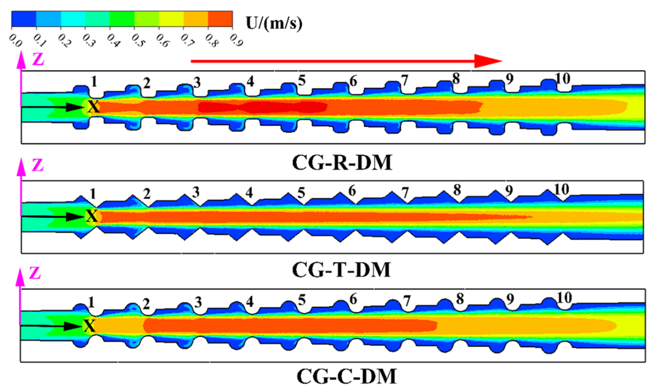


**Figure 11:** Effect of composite groove cross-section shape on velocity distribution on the y = 2 mm plane at 0.7 g/s.

Fig. 12a illustrates the influence of the composite groove cross-sectional shape on the fluid pressure distribution along the interface wall at 0.7 g/s. Higher fluid pressure on the interface wall indicates stronger direct fluid impingement of on the wall, resulting in a thinner fluid boundary layer. Among the configurations studied, the rectangular composite groove in CG-R-DM exhibits the steepest curvature, leading to the strongest direct fluid impingement. In contrast, the triangular composite grooves in CG-T-DM have the smoothest curvature, resulting in weaker impingement. Consequently, compared with CG-C-DM and CG-T-DM, CG-R-DM effectively reduce the fluid boundary layer thickness and enhance convective heat transfer between the wall and the fluid by virtue of its rectangular composite grooves. Fig. 12b illustrates the effect of composite groove cross-section shape on *Nu* distribution along the interface wall at 0.7 g/s. At each composite groove, CG-R-DM is the highest *Nu*, followed by CG-C-DM and then CG-R-DM, which corroborates the analyzes in Figs. 11 and 12a.

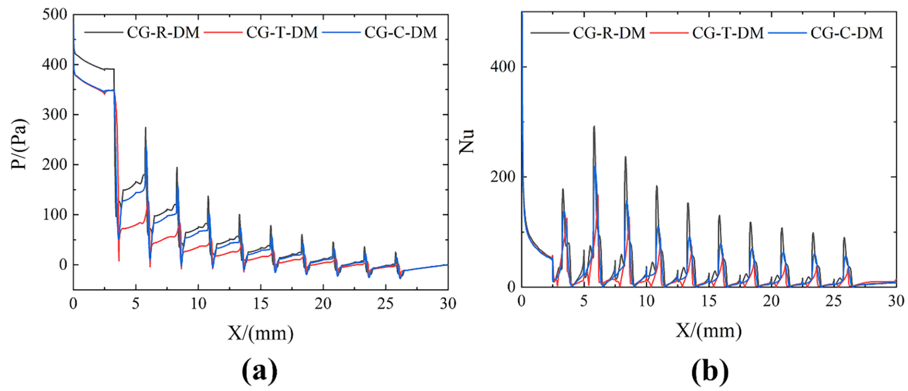


**Figure 12:** Effect of composite groove cross-section shape on pressure and *Nu* distribution on the y = 2 mm interface wall at 0.7 g/s, (**a**) pressure distribution and (**b**) *Nu* distribution.

Fig. 13 compares the temperature distribution on the y = 2 mm plane and the x = 30 mm (outlet plane) plane at 0.7 g/s. On the y = 2 mm plane, along the fluid flow direction, the temperature variation in the solid domain of CG-R-DM is smoother, whereas that in CG-T-DM more rapid. In addition, the average temperature of the near-wall fluid is lower in CG-R-DM and higher in CG-T-DM. The small temperature difference between the near-wall fluid and the interface wall in CG-T-DM increases the convective heat transfer resistance, which hinders heat dissipation from the solid domain. On the x = 30 mm plane, the low-temperature fluid region in CG-R-DM is the smallest, and average fluid temperature is the highest. In contrast, although locally high-temperature fluid exists at the outlet plane of CG-T-DM, it does not effectively increase the average fluid temperature, and the low-temperature region remains the largest. This is primarily attributed to the weak fluid disturbance in CG-T-DM, which hinders sufficient mixing between the high-temperature fluid near the wall and the cold fluid in the mainstream.

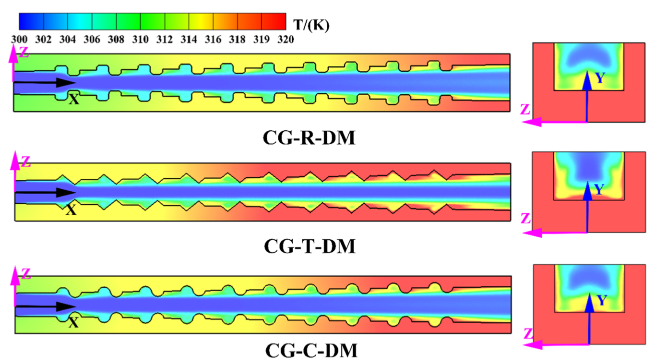


**Figure 13:** Effect of composite groove cross-section shape on temperature distribution on the y = 2 mm and outlet planes at 0.7 g/s.

Fig. 14a–c shows the effect of composite groove cross-section shape on $\Delta P$, $T_{b,ave}$, and $R_T$ at 0.3–1.1 g/s. As illustrated in Fig. 14a, differences in $\Delta P$ among CG-R-DM, CG-T-DM, and CG-C-DM arise from variations in fluid impingement on the wall. As illustrated in Fig. 14b, $T_{b,ave}$ decreases with increasing mass flow rate for all three configurations. This trend is closely associated with enhanced convective heat transfer induced by the higher mass flow rate (reducing the thickness of the fluid boundary layer). Across the studied flow range, CG-T-DM exhibits the largest $T_{b,ave}$, while CG-R-DM exhibits the lowest $T_{b,ave}$. Specifically, compared to CG-T-DM, CG-R-DM achieves an average reduction in $T_{b,ave}$ of 8.4%, indicating better cooling for the microchannel. As shown in Fig. 14c, CG-R-DM achieves the lowest $R_T$ owing to the enhanced mixing of hot and cold fluids in the near-wall region driven by fluid disturbance. In contrast, CG-T-DM exhibits the weakest fluid disturbance, resulting in the highest $R_T$.

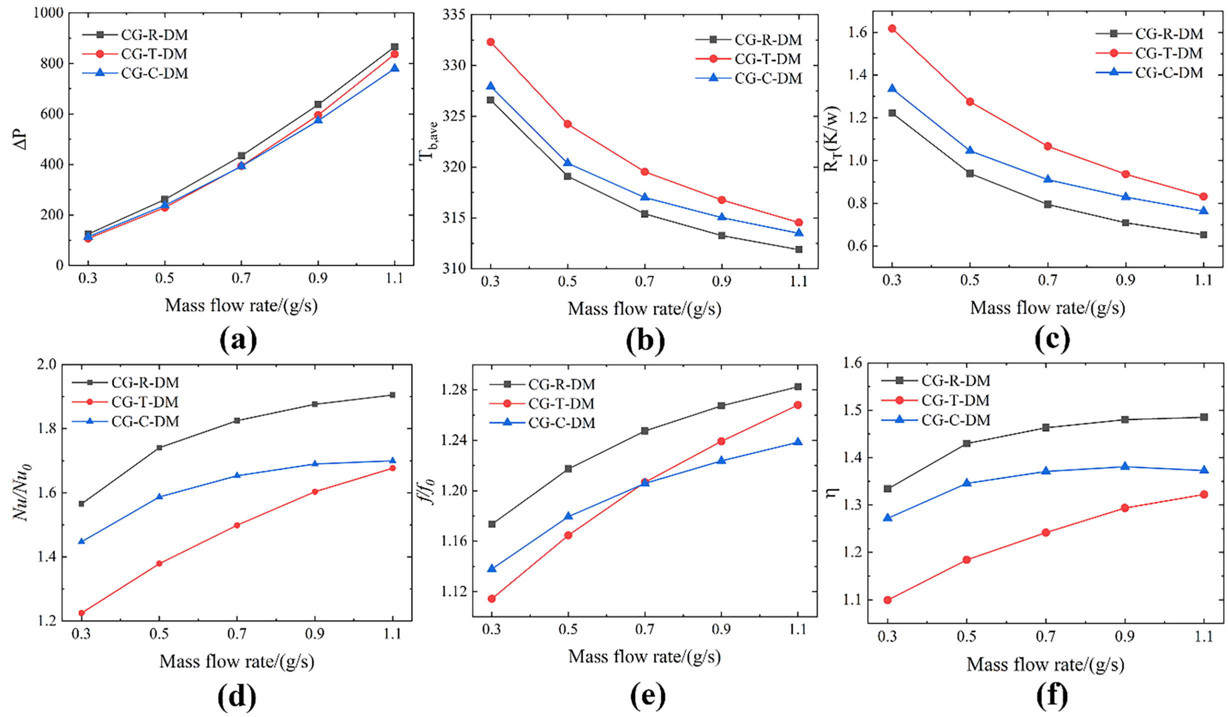


**Figure 14:** Effect of composite groove cross-section shape on hydrothermal performance indicators, (**a**) $\Delta P$, (**b**) $T_{b,ave}$, (**c**) $R_T$, (**d**) $Nu/Nu_0$, (**e**) $f/f_0$ and (**f**) $\eta$.

Fig. 14d–f illustrates the effects of composite groove cross-section shape on the ratios of $Nu/Nu_0$, $f/f_0$, and $\eta$. As shown in Fig. 14d, the $Nu/Nu_0$ ratio of CG-R-DM is higher than that of CG-T-DM and CG-C-DM at all mass flow rates. However, with the increase of mass flow rate, the $Nu/Nu_0$ ratio in CG-T-DM maintains a nearly constant increasing trend, while the increasing trend of $Nu/Nu_0$ ratio in CG-R-DM and CG-C-DM gradually slows down. This phenomenon is associated with the varying effects of composite grooves with different cross-sectional shapes on the fluid boundary thickness in CG-R-DM, CG-T-DM, and CG-C-DM. Specifically, in CG-T-DM, a higher fluid velocity is required to achieve the same level of fluid impingement intensity on the wall as that observed in CG-R-DM and CG-C-DM at low fluid velocity. As shown in Fig. 14e, the $f/f_0$ ratio relationships of CG-R-DM, CG-T-DM, and CG-C-DM are similar to the $\Delta P$ relationships presented in Fig. 14a. Furthermore, the differences in the $f/f_0$ ratios among the three configurations are significantly smaller than those in the $Nu/Nu_0$ ratio. Therefore, the difference in η between CG-R-DM, CG-T-DM, and CG-C-DM is similar to the difference in $Nu/Nu_0$ ratio, as shown in Fig. 14f. CG-R-DM can achieve the strongest hydrothermal comprehensive performance. In addition, the average η of CG-R-DM is increased by about 20% compared to CG-T-DM. This result indicates that by modifying the composite groove cross-sectional shape to enhance fluid disturbance and fluid impingement intensity on the groove walls, the heat transfer performance of microchannels can be significantly improved with a minimal increase in pressure drop.

Fig. 15 shows the effects of composite groove cross-section shape on the entropy generation indicators. As shown in Fig. 15a, due to the small difference in fluid pressure drop, the effects of CG-R-DM, CG-T-DM, and CG-C-DM on $S_F$ are also relatively small. However, there is a significant difference in $S_T$ between CG-R-DM, CG-T-DM, and CG-C-DM, as illustrated in Fig. 15b. Specifically, compared with CG-T-DM, the average $S_T$ of CG-R-DM and CG-C-DM decreased by 23.3% and 13.5%, respectively. Thus, it can be observed from Fig. 15c that among the microchannels with three different composite groove cross-sections, CG-R-DM has the lowest $S_G/S_{G0}$ ratio, followed by CG-C-DM and CG-T-DM, respectively. This indicates that CG-R-DM can achieve an overall efficiency improvement with the lowest energy consumption.

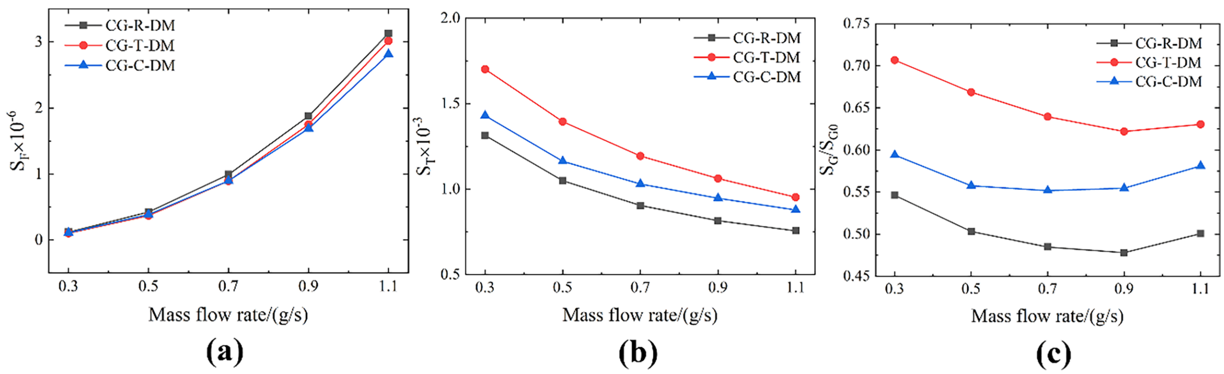


**Figure 15:** Effect of composite groove cross-section shape on entropy generation indicators, (**a**) $S_F$, (**b**) $S_T$ and (**c**) $S_G/S_{G0}$.

Therefore, due to its stronger boundary layer destruction capability, and better flow disturbance effect, the rectangular cross-sectional composite groove has a significantly higher heat transfer enhancement benefit than the penalty of increased flow resistance, thus achieving the optimal comprehensive hydrothermal performance. In contrast, the triangular cross-sectional composite groove exhibits the worst hydrothermal performance due to its weak flow disturbance, and the easy formation of a bottom dead zone, resulting in limited heat transfer improvement.

### *3.3 Comparison with Other Related Works*

The above analysis indicates that CG-R-DM achieves the optimal hydrothermal performance. To further validate the significance of this work, a comparison with existing literature is conducted. Fig. 16 compares the hydrothermal performance of the present work with that of related studies, including fan-shaped ribs [39], divergent minichannels with ribs [33], rectangular microchannels with rectangular grooves [32], and divergent microchannels with inclined grooves [23]. Although the enhancement achieved by coupling divergent microchannels with composite grooves is less pronounced than that of divergent microchannels with inclined grooves at *Re* > 300, it already surpasses other heat transfer enhancement methods. Moreover, at *Re* < 300, the proposed coupling achieves the best hydrothermal performance. Therefore, coupling divergent microchannels with composite grooves offers greater advantages for heat transfer enhancement at low *Re*.

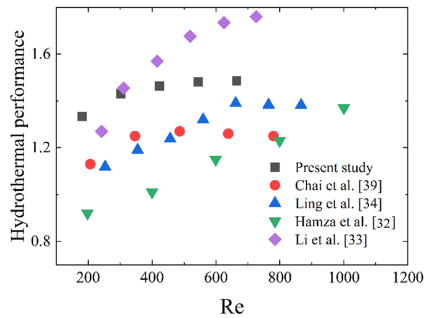


**Figure 16:** Comparison of hydrothermal performance with other related works.

## 4 Conclusions

In this work, a coupling design of grooves and microchannels is proposed to enhance the hydrothermal performance of MCHS. Systematic investigations are conducted under an mass flow rate range of 0.3–1.1 g/s focusing on two aspects: (1) the coupling modes between grooves (simple and composite) and microchannels (straight, convergent, and divergent); and (2) the effects of composite groove cross-sectional shapes (rectangular, triangular, and circular arc) on hydrothermal performance and entropy production. The following conclusions can be drawn from this research:

(1) For SG-R-SM and CG-R-SM, compared to simple grooves, composite grooves induce stronger spiral fluid disturbances between the mainstream and the near-wall zone, enhance direct fluid impingement on groove walls, improve the cooling effect on microchannels, and reduce the entropy generation.

(2) Among CG-R-SM, CG-R-CM, and CG-R-DM, CG-R-CM exhibits the strongest heat transfer performance and the lowest entropy production. Specifically, at 1.1 g/s, the maximum $Nu$ reaches 2.38, whereas the minimum $S_G$ is only 0.0015. However, while CG-R-CM significantly enhances heat transfer efficiency, it also results in a friction coefficient that is more than one order of magnitude higher than those of CG-R-SM and CG-R-DM. CG-R-DM achieves a balance between heat transfer and pressure drop, resulting in the maximum $\eta$ of 1.485 at 1.1 g/s.

(3) By leveraging cross-sectional shape differences of composite grooves to enhance fluid impingement on groove walls, heat transfer performance can be significantly improved with a slight increase in pressure drop. CG-R-DM exhibit superior effects on hydrothermal performance and entropy generation compared to CG-T-DM and CG-C-DM.

The numerical simulations in this study are based on two key assumptions: steady-state flow and constant thermophysical properties of the working fluid. Consequently, the research results do not apply to scenarios involving unsteady-state flow, phase-change heat transfer, or fluid temperature changes exceeding 50 K. Although simplified assumptions such as constant and uniform bottom heat flux, adiabatic top boundary, and constant thermophysical properties of the fluid make the computational model easier to converge and significantly improve the solution efficiency, they will also introduce certain deviations. The optimized results need to be verified through experimental tests. In future work, structural parameters such as microchannel divergence rate and composite groove curvature can be further optimized based on surrogate models (e.g., response surface models, neural network models) to achieve optimal hydrothermal performance and entropy generation of MCHS. In addition, numerical simulations did not consider manufacturing feasibility and cost, and relevant experimental tests should be conducted to evaluate the feasibility of practical applications.

**Acknowledgement:** Not applicable.

**Funding Statement:** The work is supported by the Open Project of Sichuan Engineering Research Center for Titanium Alloy Advanced Manufacturing Technology (TM-2024-Y-03) and the University-level scientific research project of Chengdu Technological University (2025ZR008).

**Author Contributions:** Guang Wen: Investigation, Methodology, Writing—original draft. Wenling Liao: Funding acquisition, Conceptualization, Writing—review & editing. Shuaimei Lian: Visualization, Validation, Writing—original draft. Pingping Liu: Supervision. All authors reviewed and approved the final version of the manuscript.

**Availability of Data and Materials:** The data set used and/or analyzed during the current study available from corresponding authors on reasonable request.

**Ethics Approval:** The article does not include human participants and/or animals research.

**Conflicts of Interest:** The authors declare no conflicts of interest.

## References

1. Tuckerman DB, Pease RFW. High-performance heat sinking for VLSI. IEEE Electron Device Lett. 1981;2(5):126–9. doi:10.1109/EDL.1981.25367.
2. Alihosseini Y, Zabetian Targhi M, Heyhat MM, Ghorbani N. Effect of a micro heat sink geometric design on thermo-hydraulic performance: a review. Appl Therm Eng. 2020;170(4):114974. doi:10.1016/j.applthermaleng.2020.114974.
3. Hou T, Chen Y. Pressure drop and heat transfer performance of microchannel heat exchanger with different reentrant cavities. Chem Eng Process Process Intensif. 2020;153:107931. doi:10.1016/j.cep.2020.107931.
4. Hou T, Xu D. Pressure drop and heat transfer performance of microchannel heat exchangers with elliptical concave cavities. Appl Therm Eng. 2023;218:119351. doi:10.1016/j.applthermaleng.2022.119351.
5. Kumar K, Kumar P. Effect of groove depth on hydrothermal characteristics of the rectangular microchannel heat sink. Int J Therm Sci. 2021;161(4):106730. doi:10.1016/j.ijthermalsci.2020.106730.
6. Zhao C, He L, You W, Meng X, Li Z. Numerical simulation of flow and heat transfer characteristics of microchannels with ribbed structures of bionic fish fins. Int J Refrig. 2025;178(32):298–311. doi:10.1016/j.ijrefrig.2025.07.012.
7. Wang G, Wang Z, Lai L, Xie D, Zhu Y, Ding G, et al. Experimental and numerical investigation of hydrothermal performance of a microchannel heat sink with pin fins. Case Stud Therm Eng. 2024;60(6):104631. doi:10.1016/j.csite.2024.104631.
8. Chen B, Zhang C, Xu Y, Chen Z. Hydrodynamic and thermal performance of in-line strip-fin manifold microchannel heat sink. Int J Heat Mass Transf. 2023;209(5):124131. doi:10.1016/j.ijheatmasstransfer.2023.124131.
9. Manda U, Peles Y. Performance evaluation criteria of a star-shaped cross-sectional horizontal microchannel with supercritical carbon dioxide. Int Commun Heat Mass Transf. 2024;157(2):107803. doi:10.1016/j.icheatmasstransfer.2024.107803.
10. Vocale P, Morini GL. Impact of cross-section geometry on microchannel heat sink performance in the presence of slip and temperature jump boundary conditions. Int J Heat Mass Transf. 2025;251:127408. doi:10.1016/j.ijheatmasstransfer.2025.127408.
11. Tan Z, Jin P, Zhang Y, Xie G. Flow and thermal performance of a multi-jet twisted square microchannel heat sink using CuO-water nanofluid. Appl Therm Eng. 2023;225(5):120133. doi:10.1016/j.applthermaleng.2023.120133.
12. Yuan Y, Liu W, Huang P, Wu N, Li C. Thermal-hydraulic performance and multi-objective design optimization of a microchannel heat sink with hollow twisted tapes. Int J Heat Fluid Flow. 2025;116(4):109993. doi:10.1016/j.ijheatfluidflow.2025.109993.
13. Li Z, Liang Y, Zhou J, Yuan D, Feng Z. Mechanism of flow boiling heat transfer enhancement in minichannels with double twisted tape inserts: experimental and numerical investigations. Int J Heat Mass Transf. 2025;252(1):127484. doi:10.1016/j.ijheatmasstransfer.2025.127484.

14. Liu Z, Shan L, Li W. Enhanced thermal performance of mini-tube with chained-jet-chamber insert. Int J Therm Sci. 2025;211:109701. doi:10.1016/j.ijthermalsci.2025.109701.
15. He B, Luo X, Yu F, Li T, Wang L, Zhou J, et al. Effects of inlet subcooling on the flow boiling heat transfer performance of bi-porous mini-channels. Appl Therm Eng. 2023;229:120577. doi:10.1016/j.applthermaleng.2023.120577.
16. Ho CJ, Peng JK, Yang TF, Rashidi S, Yan WM. On the assessment of the thermal performance of microchannel heat sink with nanofluid. Int J Heat Mass Transf. 2023;201:123572. doi:10.1016/j.ijheatmasstransfer.2022.123572.
17. Ho CJ, Peng JK, Yang TF, Rashidi S, Yan WM. Assessment of cooling performance of mini/micro-channel stacked double layer heat sink. Alex Eng J. 2023;80(6):465–74. doi:10.1016/j.aej.2023.08.074.
18. Ghadhban FN, Jaffal HM. Numerical investigation on heat transfer and fluid flow in a multi-minichannel heat sink: effect of channel configurations. Results Eng. 2023;17(5):100839. doi:10.1016/j.rineng.2022.100839.
19. Ho CJ, Chang PC, Yan WM, Amani P. Thermal and hydrodynamic characteristics of divergent rectangular minichannel heat sinks. Int J Heat Mass Transf. 2018;122:264–74. doi:10.1016/j.ijheatmasstransfer.2018.01.122.
20. Khoshvaght-Aliabadi M, Ghodrati P, Mahian O, Tae Kang Y. Enhancing the performance of supercritical $CO_2$-cooled heat sink by converging–diverging minichannels. Appl Therm Eng. 2023;234(5):121225. doi:10.1016/j.applthermaleng.2023.121225.
21. Sarvar-Ardeh S, Rafee R, Rashidi S. A comparative study on the effects of channel divergence and convergence on the performance of two-layer microchannels. Exp Tech. 2023;47(1):109–22. doi:10.1007/s40799-022-00546-9.
22. Qi P, Jing D. Experimental and numerical study on the hydrothermal performances of a mirror Y-shaped convergent mini-channel heat sink. Case Stud Therm Eng. 2024;53(6):103966. doi:10.1016/j.csite.2023.103966.
23. Jia F, Li S, Wei M, Tian M. Numerical study on hydrodynamic characteristics and heat transfer enhancement of gas-liquid Taylor flow in divergent microchannels. Chem Eng Res Des. 2025;215:263–73. doi:10.1016/j.cherd.2025.01.044.
24. Zhu Q, Cui Y, Zeng J, Zhang S, Wang Z, Zhao T. Local hydrothermal characteristics and temperature uniformity improvement of microchannel heat sink with non-uniformly distributed grooves. Case Stud Therm Eng. 2023;47(5):103113. doi:10.1016/j.csite.2023.103113.
25. Bian Y, Chen Z, Li Z, Liang Y, Li Y, Lu X, et al. Experimental investigation on the effects of inclined grooves on flow boiling heat transfer and instability in a minichannel heat sink. Int J Heat Mass Transf. 2025;236(5):126333. doi:10.1016/j.ijheatmasstransfer.2024.126333.
26. Lai Y, Ding J, Liu L. Numerical investigation on the cooling performance of lithium-ion battery using liquid cooled-plate with integrated grooves and secondary microchannel structures. Int J Therm Sci. 2025;217(7):110094. doi:10.1016/j.ijthermalsci.2025.110094.
27. Haque I, Ali N, Alam T, Siddiqui TU, Ahmad Ansari M, Yadav J, et al. Optimization of semi-pendeloque grooved in micro-channel heat sinks for thermal management under optimal pumping power. Therm Sci Eng Prog. 2025;61:103531. doi:10.1016/j.tsep.2025.103531.
28. Liu L, Zhang L, Zhang X, Xu H, Zhang H, Zhou S, et al. Thermohydraulic performance of the microchannel heat sinks with three types of double-layered staggered grooves. Int J Therm Sci. 2024;201(5):109032. doi:10.1016/j.ijthermalsci.2024.109032.
29. Liu H, Duan W. Analysis of thermohydraulic performance in periodic groove–rib microchannels based on field synergy principle. J Therm Anal Calorim. 2024;149(2):609–23. doi:10.1007/s10973-023-12663-7.
30. Mao Q, Gu Y. Heat transfer performance of inlet/outlet manifold configurations and bottom wall cavities composite in microchannel heat sinks. Int J Heat Fluid Flow. 2025;115(6):109894. doi:10.1016/j.ijheatfluidflow.2025.109894.
31. Wang Y. Numerical investigation of heat transfer enhancement in mini-channels with modified surface protrusions. Int J Heat Fluid Flow. 2025;113:109766. doi:10.1016/j.ijheatfluidflow.2025.109766.
32. Hamza NAA, Mejbel Abed I, Said NM. Thermohydraulic performance of convergent and rectangular microchannels with rectangular grooves using silver nanofluid: numerical study. J Therm Anal Calorim. 2024;149(15):8579–96. doi:10.1007/s10973-024-13209-1.

33. Li Y, Yuan D, Bian Y, Liang Y, Lu X, Guo F, et al. Hydrothermal characteristics of inclined grooves with varying numbers and depths in straight, divergent, and convergent minichannels. Appl Therm Eng. 2025;269:125957. doi:10.1016/j.applthermaleng.2025.125957.
34. Ling B, Feng Z, Lin Q, Wang Z, Guo F, Zhang J. Comparative study on hydrothermal characteristics in straight, divergent and convergent minichannels having ribs with various heights along-channel. Int J Therm Sci. 2023;187(5):108190. doi:10.1016/j.ijthermalsci.2023.108190.
35. Raj S, Shukla A, Pathak M, Khan MK. A novel stepped microchannel for performance enhancement in flow boiling. Int J Heat Mass Transf. 2019;144:118611. doi:10.1016/j.ijheatmasstransfer.2019.118611.
36. Sajid MU, Ali HM, Sufyan A, Rashid D, Zahid SU, Rehman WU. Experimental investigation of $TiO_2$–water nanofluid flow and heat transfer inside wavy mini-channel heat sinks. J Therm Anal Calorim. 2019;137(4):1279–94. doi:10.1007/s10973-019-08043-9.
37. Abdulqadur AA, Jaffal HM, Khudhur DS. Performance optimiation of a cylindrical mini-channel heat sink using hybrid straight–wavy channel. Int J Therm Sci. 2019;146(4):106111. doi:10.1016/j.ijthermalsci.2019.106111.
38. Chai L, Xia G, Zhou M, Li J. Numerical simulation of fluid flow and heat transfer in a microchannel heat sink with offset fan-shaped reentrant cavities in sidewall. Int Commun Heat Mass Transf. 2011;38(5):577–84. doi:10.1016/j.icheatmasstransfer.2010.12.037.
39. Chai L, Xia GD, Wang HS. Parametric study on thermal and hydraulic characteristics of laminar flow in microchannel heat sink with fan-shaped ribs on sidewalls–Part 3: performance evaluation. Int J Heat Mass Transf. 2016;97:1091–101. doi:10.1016/j.ijheatmasstransfer.2016.02.075.